Morphology and stability of droplets sliding on soft viscoelastic substrates

Mathieu Oléron, Laurent Limat, Julien Dervaux, Matthieu Roché

To cite this version:

Mathieu Oléron, Laurent Limat, Julien Dervaux, Matthieu Roché. Morphology and stability of droplets sliding on soft viscoelastic substrates. 2023. hal-04064658v1

HAL Id: hal-04064658
https://hal.science/hal-04064658v1

Preprint submitted on 11 Apr 2023 (v1), last revised 5 Dec 2023 (v4)

Morphology and stability of droplets sliding on soft viscoelastic substrates.

Mathieu Oléron,[1] Laurent Limat,[1] Julien Dervaux,[1] and Matthieu Roché[1,*]
[1]*Université Paris Cité, Matière et Systèmes Complexes,*
CNRS UMR 7057, F-75013 Paris, France, EU

Abstract

Soft solids such as gels and elastomers can be compliant enough to deform when a droplet lies on their surface, in particular at the line of contact between the solid, the liquid and the atmosphere. While axisymmetric contact line motion has received a lot of attention, much less is known about droplets moving on soft substrates, a configuration often encountered in applications in which symmetry may be lost. We investigate here the dynamic properties of droplets sliding on thick viscoelastic layers. We show that the partition of energy dissipation between the liquid and the solid sets the shape and velocity of droplets. When dissipation parts equally between the liquid and the solid, droplet dynamics are similar to that of droplets on rigid substrates. In the opposite case, we observe shapes that indicate the presence of contact angle hysteresis. We compare our observations to a non-linear model of the wetting of soft solids that we proposed recently. We find the model to be in excellent agreement with our data, in particular regarding the prediction of the hysteresis that we show to be only apparent. This work opens fondamental questions on the connection between the properties of the substrate and the dynamics, shapes and fragmentation of moving droplets that are relevant to all applications where soft gel coatings may be used.

A raindrop sliding on a windshield deforms into asymmetric shapes while it moves and it often leaves liquid in its wake. This seemingly common observation illustrates the complexity encountered when studying droplet and contact line motion on solid surfaces. Model systems of this daily-life situation have received a great deal of attention as the control of droplets moving on rigid surfaces is crucial to many industrial applications. For example, the dynamics of droplets sliding down a plate inclined at an angle α with the horizontal at velocity U depends on a balance of viscous, gravitational and capillary stresses. Dimensional analysis of the problem for a liquid with viscosity η, density ρ and surface tension γ shows that two dimensionless quantities, the capillary number $Ca = \eta U/\gamma$ and the Bond number $Bo_\alpha = \rho g R_0^3 \sin\alpha/(\gamma R_c)$, encapsulate its physics. Here g is the acceleration of gravity, R_0 is the radius of the droplet, assumed to be spherical just before deposition, and R_c is the contact radius between the droplet and the substrate after deposition. The latter depends on the contact angle measured between the liquid-gas and the solid-liquid interfaces inside the droplet. Experiments performed on surfaces with small contact angle hysteresis, *i.e.* a small difference between the contact angle θ_a above which the contact line starts advancing and its counterpart θ_r when receding, confirm the prediction $Ca \propto Bo_\alpha$ [1, 2]. These deceptively simple objects adopt non-trivial shapes as their velocity increases. For example, corners and cusps form at their trailing-edge [1–5] that destabilize into rivulets breaking up into small droplets known as pearls at the largest attainable velocities [1–3, 6–8]. This shape diagram challenged our theoretical understanding of wetting [9–13] and led to new insights into the dynamics of curved contact lines.

Soft visco-elastic solids such as gels are used in an increasing number of applications as coatings to control wetting and adhesion [14–16]. The deposition of a droplet induces a deformation of these soft substrates in the vicinity of the contact line, known as a ridge [17–20], the height of which is proportional to the elastocapillary length scale $\ell_s = \gamma_s/(2\mu_0)$, with γ_s and μ_0 the surface energy and the shear modulus of the solid respectively. Propagation of the ridge accompanies contact line motion, resulting in energy dissipation in both the liquid and the substrate and a slowing-down of droplets compared to the case of a rigid solid [21]. The dependence of the height of the ridge on the geometry and mechanical state of the substrate leads to susbtrate-droplet and droplet-droplet interactions that are unobtainable on rigid substrates [22–26]. However, little to nothing is known regarding the dependence of the shape and stability of droplets on their velocity when they move on a soft layer, to the best of our knowledge.

A supplementary dimensionless number, the relaxation ratio $\mathcal{R}$, characterizes droplet motion on soft substrates. This quantity indicates how dissipation parts between the liquid and the substrate [27, 28]. Here, we use a silicone gel, the rheology of which is well described by the Chasset-Thirion model [29] (see Materials and Methods). In this model, a single relaxation time τ characterizes the mechanical response. If we compare the strain-relaxation velocity induced by capillarity in the liquid, $U_l = \gamma/\eta$, to that in the solid, $U_s = \ell_s/\tau$, we obtain:

$$\mathcal{R} = \frac{\gamma\tau}{\eta\ell_s}. \tag{1}$$

Small values of $\mathcal{R}$ indicate that relaxation is slower in the liquid than in the solid, *i.e.* energy is dissipated in the droplet rather than in the solid. Wetting dynamics has been studied mostly in the limit $\mathcal{R} \to \infty$ in the literature [30, 31], when energy dissipation in the liquid can be neglected. This paper investigates the influence of $\mathcal{R}$ on the dynamics and shapes of sliding drops.

RESULTS

The most obvious signature of a change in the magnitude of the relaxation ratio lies in the shape of droplet (Fig. 1). While droplets remain nearly axisymmetric at small Bond numbers, symmetry is lost as Bo_α increases. When $\mathcal{R} \simeq 2$, a corner appears at the trailing edge. Its radius of curvature is smaller than that of the leading edge of the droplet. In contrast, the aft and fore radii of curvature are comparable when $10^2 \leq \mathcal{R} \leq 10^4$. Besides, the droplet contour contains portions parallel to the direction of motion, leading to shapes similar to those observed in the case of droplets sliding on hysteretic surfaces [6, 32–34]. A further increase of Bo_α at all values of $\mathcal{R}$ leads to the observation of the pearling instability.

Figure 2a shows that, for equivalent Bond numbers, capillary numbers vary over four orders of magnitude as the relaxation ratio changes. The data for $\mathcal{R} \simeq 2$ suggest an affine relation between Ca and Bo_α (Fig.2b), with a non-zero y-intercept, similar to the rigid case [1, 2]. The functional form for the other datasets is more complex. We multiply $\mathcal{R}$ with Ca to obtain a capillary number for the solid, $Ca_s = U\tau/\ell_s$ and plot the data in Figs. 2a and b as a function of this quantity. Accounting for variations of the equilibrium contact angle θ_{eq} from one system to another (see Supplementary Materials), we observe that the large-$\mathcal{R}$ data collapse on a single master curve (Fig. 2c). We can discriminate the curve obtained for $\mathcal{R} \simeq 2$ from the others, in line with the assumption that the power balance relevant to these experiments differs from the one tested in this representation.

Another way to characterize the dynamics of sliding droplets is to measure the dependence of the dynamic contact angle on droplet velocity. Figure 3 shows the deviation from the equilibrium contact angle θ_{eq} (see Table I) as a function of the capillary number Ca, for each system. We observe that the apparent dynamic contact angle θ_d increases smoothly as the capillary number goes from negative to positive values when $\mathcal{R} \simeq 2$. Corners appear when $Ca \geq 7.5 \times 10^{-3}$, a value of the same order of magnitude as those reported for fluoropolymer-coated silicon wafers [1–3]. The other curves display a steep jump of several tens of degrees around $Ca = 0$ that brings to mind results obtained in the case of significant wetting hysteresis [35] and when a contact line moves on low-modulus natural rubber and *cis*-butadiene [36].

In a vein similar to what we observed in figure 2, the datasets collapse on a master curve when plotted against the solid capillary number Ca_s (inset in Fig. 3). The curve obtained at $\mathcal{R} \sim 10^4$ displays plateaus in the advancing and receding branches, similar to those reported in earlier studies [27]. In contrast to Fig. 2b, the $\mathcal{R} \simeq 2$ dataset is hardly discriminable.

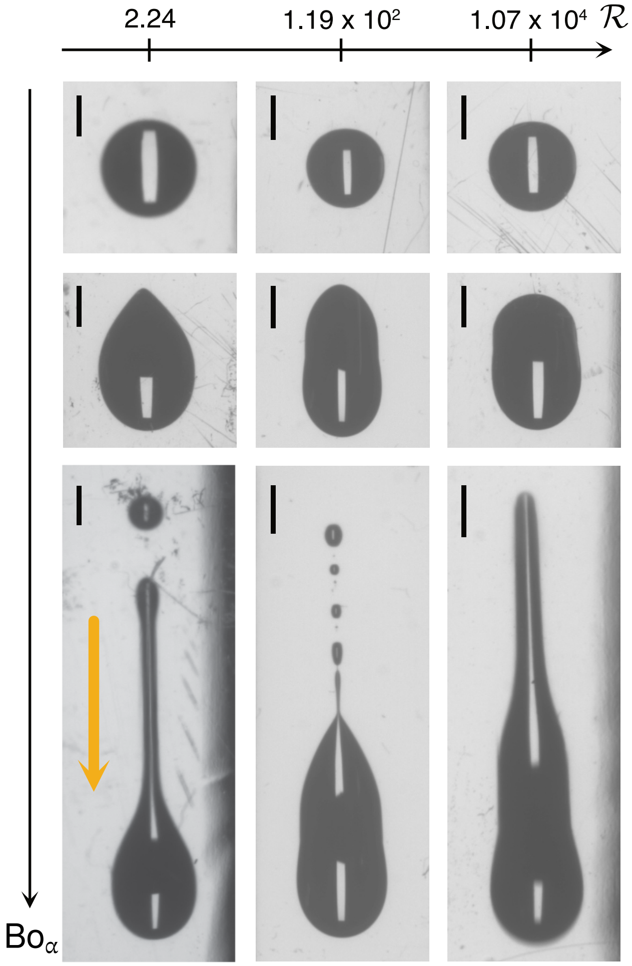

FIG. 1. **Shapes as a function of the Bond number Bo_α for different values of the relaxation ratio $\mathcal{R}$.** For each system, the drop becomes more asymetric and eventually unstable as Bo_α increases. $\mathcal{R} = 2.24$: $Bo_\alpha = 0.095$, 0.239, 0.409; $\mathcal{R} = 1.19 \times 10^2$: $Bo_\alpha = 0.103$, 0.480, 0.496; $\mathcal{R} = 1.07 \times 10^4$: $Bo_\alpha = 0.107$, 0.404, 0.442. The equivalent radius R_0 of the droplets is of the order of the capillary length $\ell_c = (\gamma/(\rho g))^{1/2}$ of the liquids in all cases. The pinch observed behind the front of the droplet at large $\mathcal{R}$ is a visual artefact: the equilibrium contact angle is greater than $\pi/2$ for these systems (see table I) and the liquid/air interface hangs over the contact line during sliding. Orange arrow in the bottom left picture: direction of motion. Scale bar: 2 mm. ©(2022) M. Oléron *et al.* (DOI: 10.6084/m9.figshare.21583407) CC BY 4.0 license https://creativecommons.org/licenses/by/4.0/.

DISCUSSION

Droplet dynamics

The data presented in figure 2 can be discussed in terms of scaling laws. We focus first on the case $\mathcal{R} \simeq 2$, and we follow a rationale that was proposed in earlier studies of droplets sliding on rigid substrates [1, 2]. We assume that dissipation occurs entirely in the liquid and balances the gravitational force experienced by the droplet. Contact-angle hysteresis may also be present. The

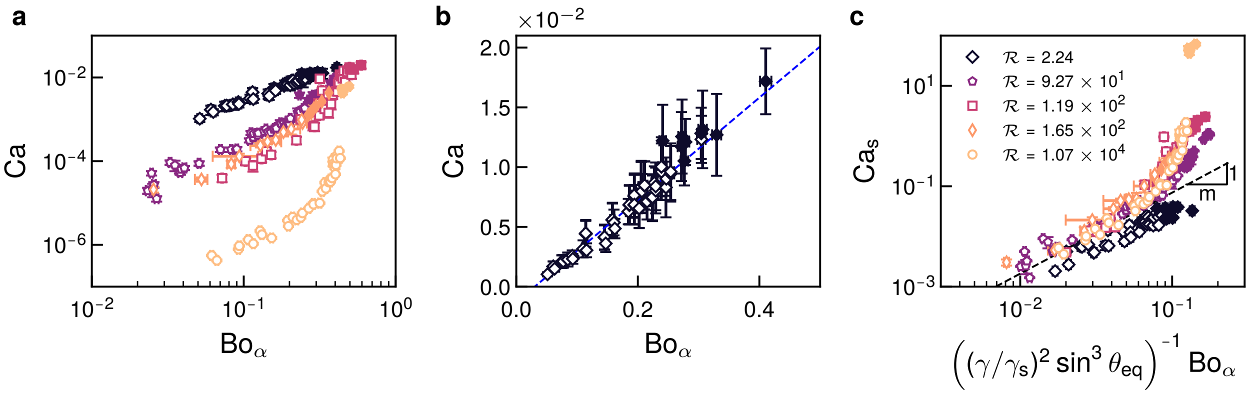

FIG. 2. **$\mathcal{R}$ impacts the relationship between droplet velocity and weight.** In all panels, filled symbols correspond to points measured above the pearling threshold. (a) Dependence of the liquid capillary number Ca on the Bond number Bo_α. (b) Focus on the case $\mathcal{R} \simeq 2$. Blue dashed line: Eq. 2. (c) Dependence of the solid capillary number Ca_s on the Bond number Bo_α. The latter is corrected for the effect of the equilibrium contact angle θ_{eq}. Dashed line: Eq. 35. ©(2022) M. Oléron *et al.* (DOI: 10.6084/m9.figshare.21583098).

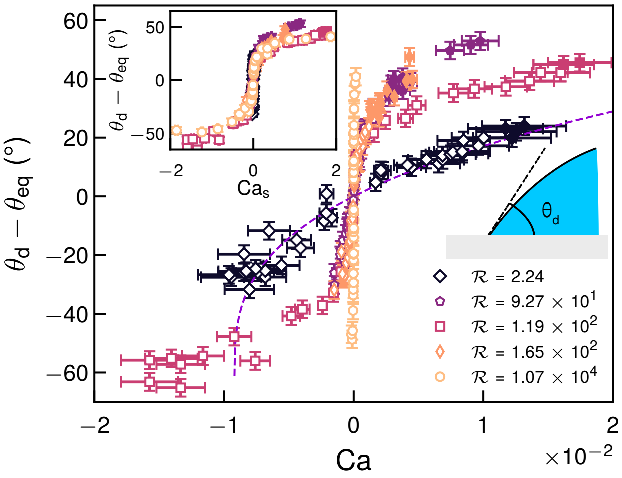

FIG. 3. **Dependence of the dynamic contact angle on droplet velocity. Experimental evidence for soft hysteresis.** Difference between the dynamic contact angle θ_d and the equilibrium contact angle θ_{eq} as a function of the liquid capillary number Ca. Positive (resp. negative) Ca values correspond to leading-edge (resp. trailing-edge) angles, and advancing (resp. receding) contact lines. In all panels, filled symbols correspond to points measured above the pearling threshold. Purple dashed line : Cox-Voinov law (Eq. 4), fitted to the data for $\mathcal{R} \simeq 2$. Inset: Same data as a function of the solid capillary number $Ca_s = \mathcal{R}Ca$. The schematic depicts how θ_d is measured between the solid/liquid and the liquid/vapor interfaces inside the droplet. ©(2022) M. Oléron *et al.* (DOI: 10.6084/m9.figshare.21583437).

resulting force balance leads to (see Supplementary Materials):

$$Ca \sim \frac{1-\cos\theta_{eq}}{\sin\theta_{eq}}\left[Bo_\alpha - Bo_c\right]. \tag{2}$$

where Bo_c is a threshold Bond number capturing hysteresis effects. Scaling 2 captures well the trend of the data obtained for $\mathcal{R} \simeq 2$ (Fig. 2c). Following arguments developed in ref. [37] and used in ref. [2], we can estimate the magnitude of the contact angle hysteresis of silicone gels from Bo_c and we find $\Delta\theta = \theta_a - \theta_r \simeq 3.5\ ^\circ$, a small value compatible with the data displayed in Fig. 3 and the rounded shapes of droplets at $\mathcal{R} \simeq 2$ (Fig. 1).

In the limit $\mathcal{R} \to \infty$, energy dissipates in the substrate. A reasoning similar to the one used in the previous paragraph leads to a scaling that balances viscous dissipation in the solid and droplet weight (see Supplementary Materials):

$$Bo_\alpha \sim \left(\frac{\gamma}{\gamma_s}\right)^2 (\sin\theta_{eq})^3 {Ca_s}^m. \tag{3}$$

For systems where $\mathcal{R} \geq 10^2$, Eq. 35 captures our data up to $Bo_\alpha \simeq 8 \times 10^{-2}$ (Fig. 2c).

Contact angles

Given the similarities between the $\mathcal{R} \simeq 2$ data and the rigid case, we compare the contact angle dependence on the capillary number to the Cox-Voinov law [2, 38, 39]:

$$\theta_d^3 - \theta_{eq}^3 = 9Ca \ln\left(\frac{h}{\lambda}\right), \tag{4}$$

where h is the height on the liquid/vapor interface at which the angle is measured and λ is a nanoscopic length scale introduced to circumvent stress divergence at the contact line. The agreement is qualitatively excellent (dashed line in Fig. 3), provided the logarithmic term has an amplitude around 15. As we measure the contact angle at $h \sim 100\ \mu\mathrm{m}$, we obtain an unreasonable cutoff length scale $\lambda \simeq 30\ \mathrm{pm}$, smaller than an interatomic bond. The large value of the logarithmic term likely results from the fact that $\mathcal{R} \sim 1$: dissipation in the solid is of the same order of magnitude as in the liquid. Failure of the Cox-Voinov law is then expected, as it does not account for all dissipation sources.

We use the $\theta_d(Ca)$ curves in Fig. 3 to test the predictions of a model that we proposed recently [28] and that describes the wetting of soft solids in a regime of finite strains. We also assume that γ_s is independent of strain: there is no Shuttleworth effect [40]. The model provides a prediction for the dependence of the dynamic contact angle θ_d on Ca and $\mathcal{R}$:

$$g(\theta_d) = g\left(\frac{\pi}{2} + \arctan\left[\left(\frac{\sqrt{1+\mathcal{A}^2(\mathcal{R}, Ca, \Lambda)} - 1}{2}\right)^{1/2}\right]\right) + Ca \ln\left(\frac{h}{\lambda}\right), \tag{5}$$

with:

$$g(x) = \int_0^x \frac{z - \sin(z)\cos(z)}{2\cos(z)} dz, \tag{6}$$

$\mathcal{A}$ a function that accounts for the capillary and viscoelastic forces that exist at the contact line, and Λ the ratio between the thickness of the substrate and the elastocapillary length ℓ_s; here $\Lambda \to \infty$. This equation is formally similar to the most general form of the Cox-Voinov relation, where the first r.h.s. term is related to the microscopic contact angle and the second results from dissipation in the liquid [41]. In Eq. 5, the microscopic angle term is a dynamic quantity set by the response

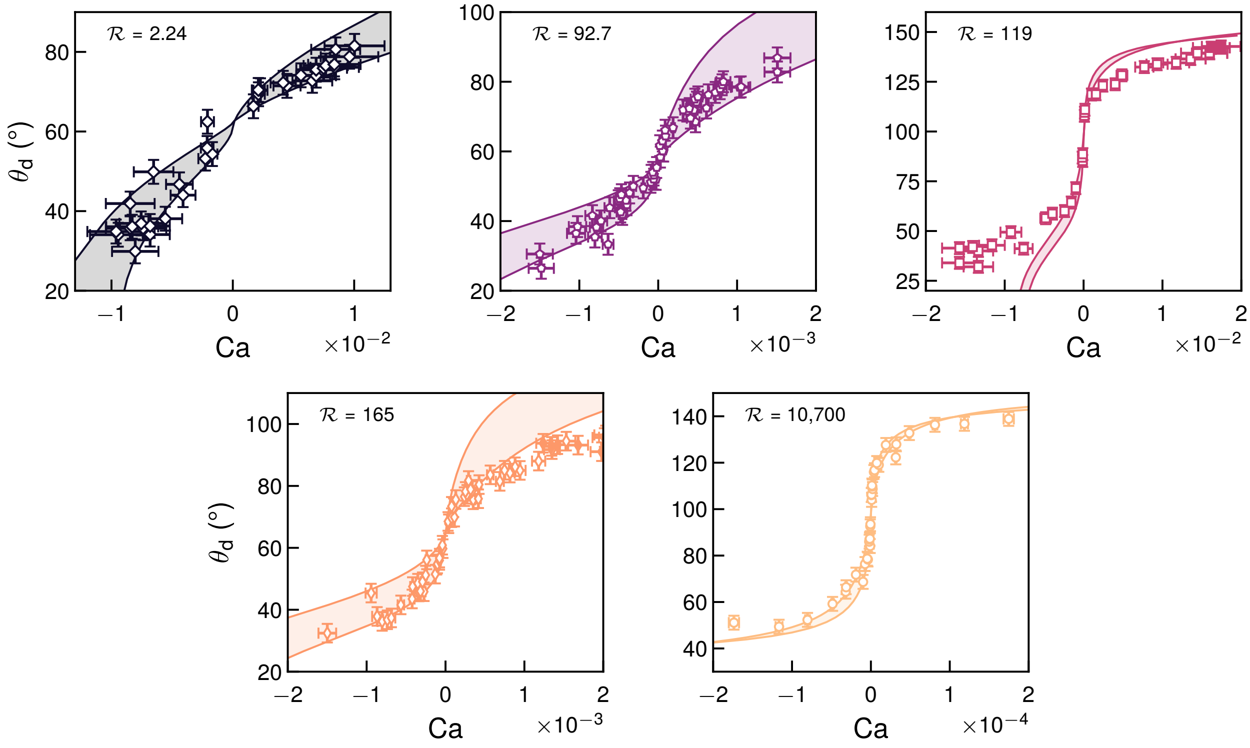

FIG. 4. **Comparison between experimental data for the dynamic contact angle θ_d and the prediction of the non-linear model.** The only fitting parameter, the microscopic cutoff length scale λ is set to 100 nm for all systems. Colored ranges show the span covered by fits if we account for uncertainties on experimental parameters at constant λ.©(2022) M. Oléron *et al.* (10.6084/m9.figshare.21583389).

of the solid to the existence and propagation of the ridge. For large relaxation ratios, the first term dominates, while the second term is prominent for vanishing $\mathcal{R}$. The model predicts a steep variation of the dynamic contact angle around $Ca = 0$ that we refer to as soft hysteresis.

Figure 4 shows comparisons between the experimental data of Fig. 3 and Eq. 5, setting $\lambda = 100$ nm. Agreement is good to excellent for all datasets. In the case $\mathcal{R} = 119$, the model fails to capture the receding branch $Ca < 0$. The steepness of the $\mathcal{R} >> 1$ curves close to $Ca = 0$ is characteristic of soft hysteresis [28]. Experiments highlight the apparent nature of this hysteresis, as contact angles remain well defined at all velocities. Despite this difference, its signature on droplet shape is akin to that of real hysteresis, as we have seen in Fig. 1. These results and their interpretation clarify the nature of the hysteresis reported for soft materials in the past literature [36], and they highlight the necessity to reach the smallest possible velocities to characterize wetting dynamics on soft solids accurately. Sliding droplets are a good system in this respect, as the sign of velocity near the contact line switches from positive to negative continuously along their contour [3, 12], providing a proxy to the relation between the dynamic contact angle and arbitrarily small droplet velocities.

The fitting procedure also suggests that all systems, even at small values of $\mathcal{R}$, exhibit a steep asymptote at $Ca = 0$. This is because viscoelastic dissipation in the solid, $\propto U^m$ with $m < 1$, always exceeds viscous dissipation in the liquid, $\propto U$, at vanishing Ca. We note that the value of $\Delta\theta$ that we obtain from Eq. 2 is compatible with the magnitude of the jump seen in the fit of the model to the data for $\mathcal{R} \simeq 2$, indicating again that manifestations of soft hysteresis in the dynamics and shapes of moving droplets is akin to that of real, defect-induced, hysteresis. The model can also predict the results displayed in Fig. 2 including the deviation from the power-law regime for large $\mathcal{R}$ (see Supplementary Materials).

Finally, fits to the datasets with Eq. 5 are obtained while keeping the microscopic cut-off length scale λ constant. We can also leave λ free to adjust, while setting experimental parameters to their nominal value (without uncertainties). We find that best-fit values lie in the range between 50 and 1000 nm, larger than the molecular sizes of the liquids we use, of the order of 10 nm at most, and smaller than the elastocapillary length $\ell_s \simeq 20\ \mu\mathrm{m}$. The large magnitude of λ could be the result of the presence of free chains that are known to lubricate the contact between the droplet and the gel and induce significant slip [15, 16, 42]. The motion of droplets is then similar to that observed on liquid-infused surfaces [43]. Our model seems to provide at least qualitative information on slip during the motion of droplets.

Transition to pearling

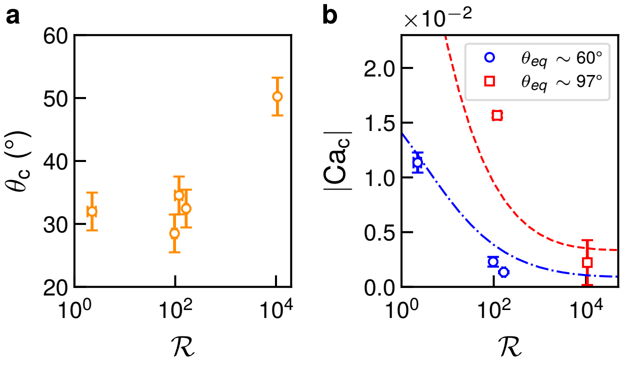

FIG. 5. **Receding contact angle θ_c and capillary number Ca_c at the pearling threshold as a function of the dissipation ratio** $\mathcal{R}$. For each system, θ_c corresponds to the receding contact angle of the last stable point, and Ca_c is the mean of the capillary numbers of the last stable and the first unstable points. Error on the latter is estimated with its standard deviation. (a) Critical receding contact angle θ_c as a function of $\mathcal{R}$. (b) Critical capillary number $|Ca_c|$ as a function of $\mathcal{R}$ for equilibrium contact angles $\theta_{eq} \sim 60$ and 97 °. Dashed lines: prediction of the non-linear model of ref. [28] for the capillary number at which the receding dynamic contact angle is zero. Values of the receding contact angle and capillary number at $\mathcal{R} \simeq 10^4$ are obtained with a larger uncertainty because the system jumps between two very different states as the threshold is passed. ©(2022) M. Oléron *et al.* (DOI: 10.6084/m9.figshare.21583275).

The characterization of the properties of the system at the threshold of the pearling instability shows how different the transition to liquid deposition on soft substrates is from that on rigid ones. First, the contact angle just before pearling, θ_c, is around 32° when the relaxation ratio $\mathcal{R} \lesssim 10^2$ and rises up to 50° when $\mathcal{R} \simeq 10^4$ (Fig. 5a). These values are much larger than those, around 10°, reported for rigid substrates [2]. Second, the threshold capillary number $|Ca_c|$ depends on both the equilibrium contact angle θ_{eq} and $\mathcal{R}$ (Fig. 5b). While the former is expected [13] and may at least partly explain the jump of around an order of magnitude in $|Ca_c|$ that we see for $\mathcal{R} \sim 100$, the latter remains to be investigated. For $\mathcal{R} \simeq 2$, $|Ca_c| \simeq 1.1 \times 10^{-2}$ and it is around twice as large as in the rigid case for a comparable equilibrium contact angle θ_{eq} [2]. Keeping the latter constant, a one-hundredfold increase of $\mathcal{R}$ decreases $|Ca_c|$ tenfold. This result stems from the fact that receding branches in the $\theta_d(Ca)$ curves tend to be steep, and their steepness increases with an increase of $\mathcal{R}$ [28]. As a consequence, for a constant equilibrium contact angle, the capillary number at which a zero receding contact angle is attained decreases as $\mathcal{R}$ increases. Thus, we expect the rivulet transition to occur at smaller values of Ca for larger values of $\mathcal{R}$. This rationale explains why the prediction of our model for the zero-contact-angle receding capillary number in figure 5b captures quite well the data. It also suggests that dissipation in the substrate increases the sensitivity of droplets to the pearling instability.

CONCLUDING REMARKS

In conclusion, we document how droplets slide on soft viscoelastic gels as a function of the partition of energy dissipation between the liquid and the substrate. While the substrate is always deformable in these experiments, sliding droplets may display shapes and dynamics akin to those observed on a rigid solid, in particular when dissipation occurs in comparable amounts in the liquid and the solid. When the latter is the main dissipative element, droplets show extended regions where portions of their contour are straight lines parallel to the direction of motion. These shapes are signatures of an apparent hysteresis that appears when the dependence of dynamic contact angles on velocity is measured. A non-linear model that we proposed recently is able to describe the data very well with a single fitting parameter, a microscopic slip length, that seems to be able to account for the lubricating effect of the free chains present in our system. Thus, accounting for geometrical non-linearities is enough to describe the dynamics of a droplet of a soft substrate, without the need for a dependence of the surface energy of the solid on strain, in line with recent experimental results [44].

This study raises fascinating questions regarding the physics of wetting, in particular with respect to the shape diagram, the existence and properties of the corner and the transition to pearling. First, cusps, *i.e.* corners characterized by a change of the sign of the curvature of the contact line, appear in our systems at the same time as the pearling stability; they are always unstable. Second, corners appear only once the droplet is unstable in systems where energy is dissipated mostly in the solid. These observations suggest the curvature of the trailing edge is constrained by the substrate and cannot become arbitrarily high. The systems we use do not allow us to ascribe a clear origin for this constraint. This issue calls for future work in which care shall be taken to discriminate effects due to free chains from those due to the cross-linked polymer network. On top of that, our data indicate that the ability to tune independently the relaxation timescale τ and the shear modulus μ_0 while keeping the viscosity of the liquid constant may be a viable route to obtain designer coatings. Investigation of the adjustment of the height of the ridge *via* gel thickness control and/or the application of pre-strains should also help improve our understanding of sliding droplets [24–26]. Besides, given the parallel that was established recently between liquid-infused surfaces [43] and polymer gels [42], it would be interesting to entirely remove the contribution of the cross-linked network to see whether the presence of a viscous liquid is sufficient to modify the appearance of corners and the transition to pearling in a way similar to the one we report. Finally, we have also observed oscillations of the trailing edge of the droplet as the system approaches the pearling transition. These oscillations may explain why the model does not fit the data well for receding contact lines at $\mathcal{R} \sim 100$, as it provides no prediction for them. These studies will open the possibility to design efficient compliant coatings.

MATERIALS AND METHODS

Liquids

We use pure glycerol (G100, Sigma Aldrich, G5516), a 60-%-glycerol-in-water mixture (G60), polyethylene glycol-ran-propylene glycol monobutyl ether (P25, PEG-ran-PPG ME, average molecular weight $M_w \sim 2500\,\mathrm{g\,mol^{-1}}$, Sigma Aldrich), a 70%-polyethylene glycol-ran-propylene glycol monobutyl ether-in-water mixture (P7, PEG-ran-PPG ME, Sigma Aldrich), and the UCON lubricant 75-H-90,000 (U90, Dow corning). Table I summarizes their properties. All the liquids are insoluble in silicone gels. We measure the liquid-vapor surface tension γ with the pendant drop technique. We estimate density ρ by weighing a volume $V = 10 \pm 0.5$ mL of liquid with a 0.01-g-accurate scale. We measure the dynamic viscosity η with a capillary viscosimeter sitting next to the set-up twice a day to account for hygroscopic and thermal effects.

TABLE I. Properties of liquids used in our experiments.

Liquid	γ	η	ρ	θ_{eq}	$\mathcal{R}$
	mN m^{-1}	mPa s	10^3 kg m^{-3}	°	
U90	40.7	36900	1.08	61.6	2.24
	± 0.9	± 690	± 0.05	± 0.7	± 0.42
P7	37.3	842	1.05	56.6	92.7
	± 0.2	± 99	± 0.05	± 0.7	± 11.0
G100	63.1	631	1.27	97.2	119
	± 0.5	± 104	± 0.06	± 1.1	± 20
P25	37.1	491	1.05	64.3	165
	± 0.4	± 34	± 0.01	± 0.2	± 11
G60	62.9	6.8	1.16	98.1	10700
	± 0.1	± 0.2	± 0.06	± 0.9	± 400

Equilibrium contact angle measurements

Wetting equilibrium is difficult to identify on these systems using classical techniques such as droplet deposition. We see the contact line moving even a few hours after deposition. We circumvent this issue by deducing equilibrium contact angles θ_{eq} from experimental dynamic contact angles (Fig 3): we fit the points around $U = 0$ with a linear law, and take θ_{eq} equal to the value of the fitted contact angle at $U = 0$.

Gel preparation

Gel slabs are prepared with a two-part commercial silicone kit (Dow Corning Sylgard 527). We mix equal volumes of each part of the kit together, as recommended by the manufacturer, in a weighing boat previously cleaned with ethanol and water, and dried. The gel mixture is degassed under vacuum for 2 h to remove bubbles. It is then poured in a 60×40-mm^2 plastic vessel (Caubère), also cleaned with ethanol and distilled water and let to dry in a vacuum before use. Then, we leave the sample in an oven at 65 °C for 15 to 18 h. We perform experiments exclusively on dust-free unmarked gels.

Free-chain extraction

We extract free chains from silicone gels using the process described in ref. [45]. After weighing pieces of gels, we dip them into toluene (VWR, AnalaR NORMAPUR), a good solvent for PDMS. Free chains migrate to the solvent. We renew toluene everyday for five days to accelerate the extraction process. Then the sample is immersed in a mixture of toluene and ethanol (VWR, AnalaR NORMAPUR) to the bath to remove toluene from the gel. Ethanol is added progressively to avoid damaging the sample. We start with a solution of 20wt% ethanol in toluene, and we increase the ethanol proportion by steps of 20wt% every day, until the sample sits in 100% ethanol. After three baths in pure ethanol, the gel stops shrinking. We dry the gel under vacuum to remove remaining solvent and weigh it again. From this procedure, we find that our materials contain 62 wt% free chains. This large amount of free chains explains likely the absence of transition between two sliding regimes [45, 46] in our experiments.

Rheology

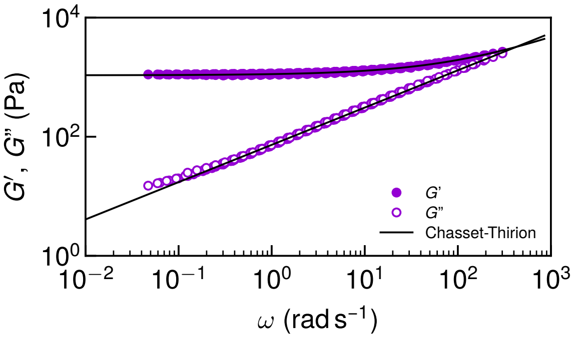

FIG. 6. **Rheology of Sylgard 527.** Storage modulus G' and loss modulus G" as function of pulsation ω. Strain amplitude: 1%. Continuous black lines: Chasset-Thirion law, Eqs. 8 and 9.

We perform small amplitude oscillatory shear rheology on our gels with an Anton Paar MCR 501 rheometer mounted with a plate-plate geometry (diameter $d = 25$ mm). Strain amplitude is set at 1%. We extend the frequency range using a time-temperature superposition procedure [47]. We fit the data with the Chasset-Thirion model [29]:

$$G(\omega) = \mu_0(1 + (i\omega\tau)^m), \tag{7}$$

with G the complex modulus, ω the strain angular frequency and τ a characteristic relaxation time. The exponent m depends on the degree of polymerization of the polymer network and on the coordination number of monomers [29, 48].

If we decompose the complex modulus $G(\omega)$ in a real elastic part $G'(\omega)$ and an imaginary dissipative part G"(ω), we obtain

$$G'(\omega) = \mu_0(1 + \cos(m\pi/2)\,(\omega\tau)^m), \tag{8}$$

$$G"(\omega) = \mu_0 \sin(m\pi/2)\,(\omega\tau)^m. \tag{9}$$

We determine τ and m by fitting the loss factor deduced from the model to its experimental value:

$$\frac{G”}{G'}(\omega) = \tan(\delta) = \frac{\sin(m\pi/2)\,(\omega\tau)^m \tan(m\pi/2)}{\sin(m\pi/2)(\omega\tau)^m + \tan(m\pi/2)}. \tag{10}$$

We inject the values of τ and m to fit equations 8 and 9 to the rheological data (Fig. 6). We find $\mu_0 = 1.077$ kPa, $\tau = 18.2$ ms, and $m = 0.626$.

Sliding experiments

We deposit a liquid droplet with a micropipette on the gel. The experiment starts when we tilt the gel at an angle α with the horizontal. A LED panel (Effilux) shines light on the sample from below, and a camera (Imaging Source, DMK 33UX174) records top views of the droplet with a spatial resolution of 32 $\mu\mathrm{m\,px}^{-1}$. We take side views on some experiments (Imaging Source, DMK 33UX174, spatial resolution 4 $\mu\mathrm{m\,px}^{-1}$). The thickness of all the samples, $h_s \sim 4$ mm, is much larger that the elastocapillary length of our material, $\ell_s \sim 10$ µm, to avoid small-thickness effects [24]. Samples are covered with a polystyrene lid that we find able to prevent surface ageing and dust deposition. We unmold gel layers and cut their edges so the meniscus is not in the way of side views. We obtain identical results when the silicone gel is in the box or unmolded.

We check the volume of droplets by weighing samples before droplet deposition and after. We tracked the motion of droplets with the software package FiJi [49]. Droplet velocities range from 10^{-3} to 1 mm s^{-1}. In most cases, the trajectories that we observe are linear functions of time: droplets move at constant speed. For the longest experiments, drops may lose or gain water from surrounding air. In that case, we fit only the part of the trajectory that is unaffected. Thus we extract a single value U of the droplet velocity from each experiment. Each set of experimental conditions is tested three times to ensure reproducibility.

SUPPLEMENTAL MATERIALS

Derivation of scaling laws describing the dynamics of sliding droplets.

Vanishing values of the relaxation ration $\mathcal{R}$

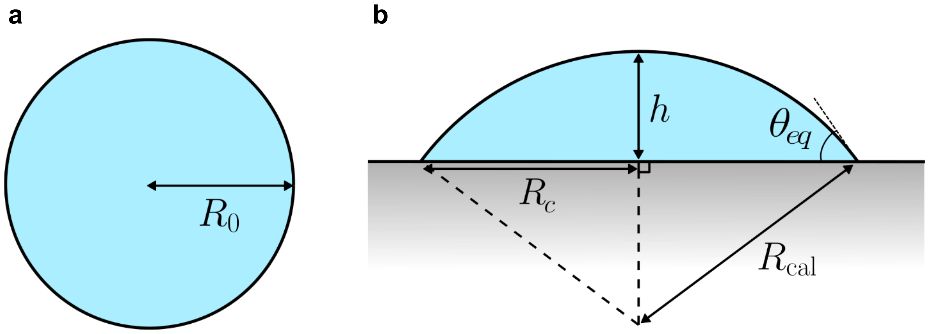

FIG. 7. **Different configurations for a liquid drop.** (a) A spherical droplet of volume $V = 4R_0^3/3\pi$. (b) The same droplet as a spherical cap after spreading on a substrate, with radius of curvature R_{cal}, height at the center h, contact radius R_c and contact angle θ_{eq}.

In experiments, a droplet of volume V is deposited on the substrate. This volume corresponds to a sphere of radius R_0 (Fig. 7a). Once it has spread on the surface of the substrate, the droplet reaches its equilibrium shape, a spherical cap with radius R_{cal}, height h, contact radius R_c and contact angle θ_{eq} (Fig. 7b).

R_c is difficult to measure in experiments, especially when the equilibrium contact angle is larger than $\pi/2$. In contrast, we can obtain R_0 by weighing the drop. If we know the equilibrium contact angle θ_{eq}, we can write, assuming that droplets form spherical caps:

$$\begin{cases} R_c = R_{\mathrm{cal}} \cos\left(\frac{\pi}{2} - \theta_{eq}\right) \\ R_{\mathrm{cal}} - h = R_{\mathrm{cal}} \sin\left(\frac{\pi}{2} - \theta_{eq}\right). \end{cases} \tag{11}$$

Rearranging, we can link the contact radius and the height of the droplet to the spherical cap radius:

$$\begin{cases} R_c = R_{\mathrm{cal}} \sin\theta_{eq} \\ h = R_{\mathrm{cal}}(1-\cos\theta_{eq}). \end{cases} \tag{12}$$

Now, we can express the volume for both a sphere and a spherical cap:

$$\begin{cases} V = \frac{4\pi}{3} R_0^3 \\ V = \frac{\pi}{3} h^2 (3R_{\mathrm{cal}} - h) \end{cases} \tag{13}$$

in terms of R_c and θ_{eq}:

$$\begin{cases} V = \frac{4\pi}{3} R_0^3 \\ V = \frac{\pi R_c^3}{3} \frac{(2+\cos\theta_{eq})(1-\cos\theta_{eq})^2}{\sin^3\theta_{eq}} \end{cases} \tag{14}$$

Volume conservation then leads to:

$$\frac{R_c}{R_0} = \frac{1}{f(\theta_{eq})} = \sin\theta_{eq}\left(\frac{(2+\cos\theta_{eq})(1-\cos\theta_{eq})^2}{4}\right)^{-\frac{1}{3}}. \tag{15}$$

For a droplet sliding down an inclined plane, the ratio between its weight and the capillary force along its perimeter, called the Bond number, writes:

$$Bo_\alpha = \frac{\rho g R_0^3}{\gamma R_c}\sin\alpha. \tag{16}$$

Injecting Eq. 15 into Eq. 16, we obtain an expression for the Bond number that accounts for changes in the equilibrium contact angle:

$$\boxed{Bo_\alpha = f(\theta_{eq})\frac{\rho g R_0^2}{\gamma}\sin\alpha.} \tag{17}$$

Now, let's assume that the gravitational force experienced by the droplet is balanced dissipation in the liquid and contact angle hysteresis:

$$\rho g R_0^3 \sin\alpha \sim \eta\frac{U}{h}R_c^2 + \gamma(\cos\theta_a - \cos\theta_r)R_c. \tag{18}$$

Here U/h estimates the velocity gradient in the droplet, and θ_a and θ_r are the advancing and receding dynamic contact angles, *i.e.* the threshold values of the contact angle above and below which contact line motion occurs.

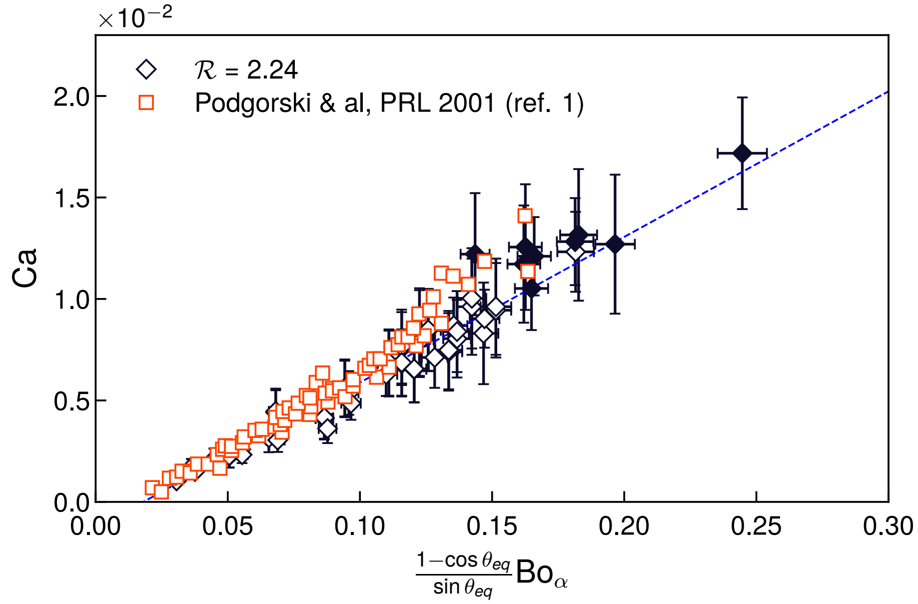

FIG. 8. Comparison between our data for $\mathcal{R} \simeq 2$ and the data of Podgorski *et al.* [1] once corrections related to a different equilibrium contact angle are accounted for.

In what follows, we assume that the values of dynamic contact angles are close to that of the equilibrium contact angle, a hypothesis that is valid at low droplet velocities, $Ca << 1$. Thus, we can use the description of the equilibrium shape of the droplet to relate the contact angle and the contact radius. Using Eq. 12, we obtain:

$$\frac{R_c^2}{h} = R_c \frac{\sin\theta_{eq}}{1-\cos\theta_{eq}} \tag{19}$$

Dividing both sides by the liquid-vapor surface tension γ, replacing R_c^2/h, and using Eq. 15, it follows that:

$$Ca \sim \frac{1-\cos\theta_{eq}}{\sin\theta_{eq}}[Bo_\alpha - Bo_c], \tag{20}$$

where Bo_c is a threshold Bond number below which contact hysteresis pins the droplet to the surface. We observe that this correction leads to the overlap of our data for $\mathcal{R} \simeq 2$ and those of ref. [1] (Fig. 8). Following Dussan [37] and Le Grand *et al.* [2], we can evaluate contact angle hysteresis from the experimental value of Bo_c using:

$$Bo_c = \left(\frac{24}{\pi}\right)^{1/3} \frac{(\cos\theta_r - \cos\theta_a)(1+\cos\theta_a)^{1/2}}{(2+\cos\theta_a)^{1/3}(1-\cos\theta_a)^{1/6}} \tag{21}$$

Le Grand *et al.* performed this estimation accounting for the prefactor appearing in front of Bo_α when fitting their data with Eq. 20. We use the same procedure to obtain our estimate.

Large-$\mathcal{R}$ sliding

We expect that the relation between injected energy and dissipation be modified when the effective viscosity of the solid exceeds that of the liquid. The collapse of the $Ca - Bo_\alpha$ curves in the $Ca_s - Bo_\alpha$ space, with $Ca_s = \mathcal{R}Ca$, suggests that the latter is a good metric. Besides, we know from the previous section that the equilibrium contact angle matters. Hence we should derive a scaling law for the solid-dominated case that accounts for all of these modifications. Note that we use again the approximation that the dynamic contact angles remain close to the equilibrium contact angle.

Inspired by Ref. [24], we estimate the power dissipated per unit of volume of the solid when the drop moves by a length ℓ:

$$d\mathcal{P}_{\text{diss}} \sim \sigma\varepsilon^2\omega \tag{22}$$

with σ the viscous stress, ε the strain and ω the pulsation. Using the Chasset-Thirion model:

$$G(\omega) = \mu_0(1+(i\omega\tau)^m), \tag{23}$$

and taking the typical strain scale to be:

$$\varepsilon \sim \frac{\gamma}{\gamma_s}\sin\theta_{eq} \tag{24}$$

and the characteristic pulsation of the experiment as:

$$\omega = \frac{U}{\ell_s}, \tag{25}$$

we have the following estimate for viscous stresses in the solid:

$$\sigma \sim \mu_0 \left(\frac{U\tau}{\ell_s}\right)^m. \tag{26}$$

Then we have:

$$d\mathcal{P}_{\text{diss}} \sim \mu_0 \left(\frac{U\tau}{\ell_s}\right)^m \left(\frac{\gamma}{\gamma_s}\sin\theta_{eq}\right)^2 \frac{U}{\ell_s} \tag{27}$$

Dissipation takes place in a half-torus having a radius R_c, width ℓ and height ℓ_r. As elasticity balances the vertical component of the resulting capillary force per unit length at the contact line $\gamma\sin(\theta_{eq})$, the height of the ridge scales as:

$$\ell_r \sim \gamma\sin\theta_{eq}/\mu_0. \tag{28}$$

Then, we can estimate the power dissipated in the solid, neglecting numerical prefactors:

$$\mathcal{P}_{\text{diss}} \sim \sigma\varepsilon^2\omega R_c\ell_r\ell \tag{29}$$

$$\mathcal{P}_{\text{diss}} \sim \mu_0 U R_c \ell \left(\frac{\gamma}{\gamma_s}\sin\theta_{eq}\right)^3 \left(\frac{U\tau}{\ell_s}\right)^m \tag{30}$$

Now, we can write the force balance that a droplet sliding on a viscoelastic substrate should obey. Dividing $\mathcal{P}_{\text{diss}}$ by the sliding velocity U, we have:

$$\rho g R_0^3 \sin\alpha \sim \mu_0 R_c \ell \left(\frac{\gamma}{\gamma_s}\sin\theta_{eq}\right)^3 \left(\frac{U\tau}{\ell_s}\right)^m. \tag{31}$$

Dividing by the liquid-vapor surface tension γ on both sides and rearranging, we obtain:

$$Bo_\alpha \sim \frac{\mu_0\ell}{\gamma} \left(\frac{\gamma}{\gamma_s}\sin\theta_{eq}\right)^3 \left(\frac{U\tau}{\ell_s}\right)^m \tag{32}$$

and using:

$$\frac{U\tau}{\ell_s} = \mathcal{R}Ca = Ca_s, \tag{33}$$

we end up with the following prediction:

$$Bo_\alpha \sim \frac{\mu_0\ell}{\gamma} \left(\frac{\gamma}{\gamma_s}\sin\theta_{eq}\right)^3 {Ca_s}^m. \tag{34}$$

The prefactor $[(\gamma/\gamma_s)\sin(\theta_{eq})]^3$ in Eq. 34 should capture the dependence on equilibrium contact angles. In the limit of thick samples, $\ell = \ell_s = \frac{\gamma_s}{2\mu_0}$ [24], and we obtain Eq. 7 in the main text when neglecting numerical prefactors:

$$Bo_\alpha \sim \left(\frac{\gamma}{\gamma_s}\right)^2 (\sin\theta_{eq})^3 {Ca_s}^m. \tag{35}$$

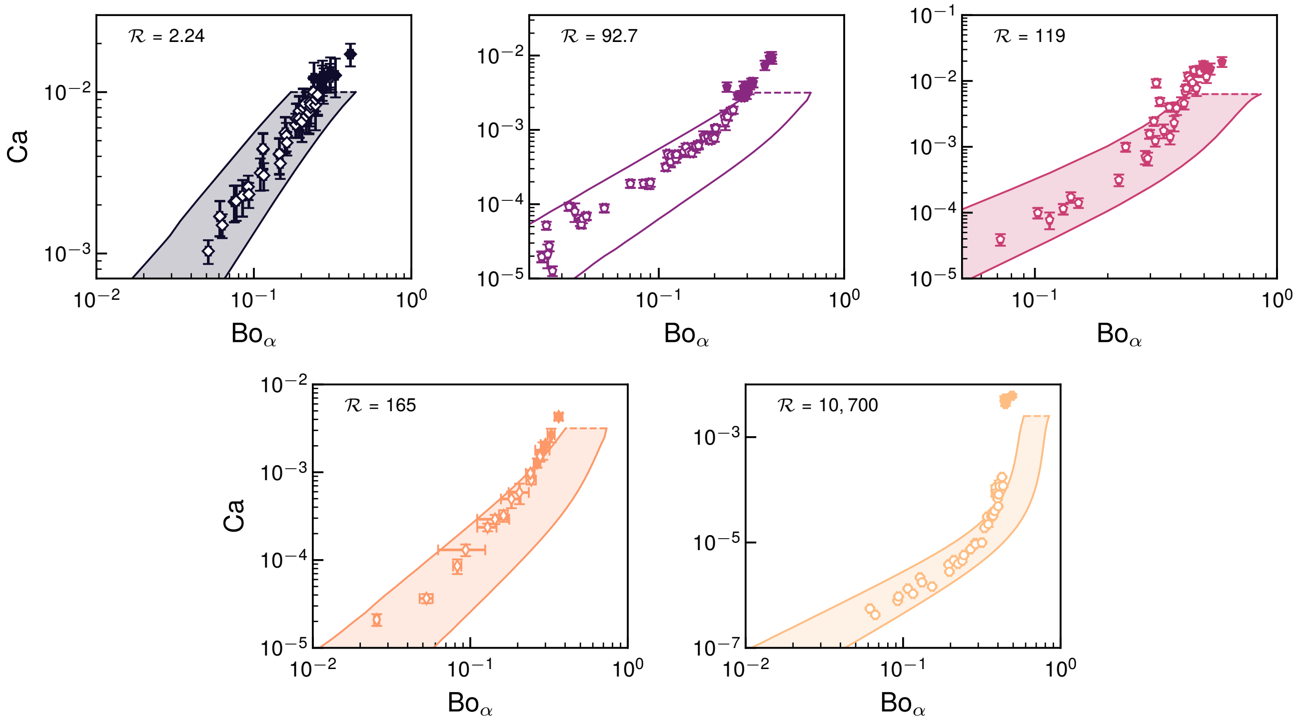

FIG. 9. Comparison between the data of Fig. 2 in the main text with the non-linear model of Dervaux *et al.* [28]. Closed symbols represent data points obtained beyond the pearling threshold. The fitting domains represent the variation of the fitting results due to uncertainty on the experimental parameters. Dashed lines: pearling threshold capillary number.

Comparison of experimental $Ca - Bo_\alpha$ curves with the non-linear model

Figure 9 shows a comparison between experimental data for the $Ca - Bo_\alpha$ displayed in Fig. 2 in the main text and theoretical predictions from our non-linear model [28]. Theoretical fits cover a surface in the $Ca - Bo_\alpha$ space because we account for uncertainties in experimental parameters such as the viscosity and the surface tension of the liquids, etc. Fits are seen to be in good agreement with experimental data.

It is our pleasure to thank Laurence Bergougnoux and Elisabeth Guazzelli for providing UCON U90. We are also very grateful to Hélène Montès for sharing her expertise on time-temperature rheology with us and performing the rheological characterization of Sylgard 527. ANR (Agence Nationale de la Recherche) and CGI (Commissariat à l'Investissement d'Avenir) are gratefully acknowledged for their financial support through the GelWet project (ANR-17CE30-0016).

---

[*] E-mail address: matthieu.roche@u-paris.fr

[1] Podgorski T, Flesselles JM, Limat L (2001) Corners, cusps, and pearls in running drops. *Phys. Rev. Lett.* 87:036102.

[2] Le Grand N, Daerr A, Limat L (2005) Shape and motion of drops sliding down an inclined plane. *J. Fluid Mech.* 541:293–315.

[3] Rio E, Daerr A, Andreotti B, Limat L (2005) Boundary Conditions in the Vicinity of a Dynamic Contact Line: Experimental Investigation of Viscous Drops Sliding Down an Inclined Plane. *Phys. Rev. Lett.* 94:024503.

[4] Peters I, Snoeijer JH, Daerr A, Limat L (2009) Coexistence of two singularities in dewetting flows: Regularizing the corner tip. *Phys. Rev. Lett.* 103:114501.

[5] Winkels K, et al. (2011) Receding contact lines: From sliding drops to immersion lithography. *Eur. Phys. J. Spec. Top.* 192:195–205.

[6] Puthenveettil BA, Senthilkumar VK, Hopfinger EJ (2013) Motion of drops on inclined surfaces in the inertial regime. *J. Fluid Mech.* 726:26–61.

[7] Kim H, Poelma C, Ooms G, Westerweel J (2015) Experimental and theoretical study of dewetting corner flow. *J. Fluid Mech.* 762:393–416.

[8] Liang W, Tietze S (2017) Pearls in running drops on an inclined glass substrate excited by Lamb waves. *Sci Rep* 7(1):14164.

[9] Thiele U, Neuffer K, Bestehorn M, Pomeau Y, Velarde MG (2002) Sliding drops on an inclined plane. *Colloids and Surfaces A: Physicochemical and Engineering Aspects* 206:87–104.

[10] Ben Amar M, Cummings LJ, Pomeau Y (2003) Transition of a moving contact line from smooth to angular. *Phys. Fluids* 15:2949–2960.

[11] Limat L, Stone HA (2004) Three-dimensional lubrication model of a contact line corner singularity. *EPL* 65:365.

[12] Snoeijer JH, Rio E, Le Grand N, Limat L (2005) Self-similar flow and contact line geometry at the rear of cornered drops. *Phys. Fluids* 17:072101.

[13] Snoeijer JH, Le Grand-Piteira N, Limat L, Stone HA, Eggers J (2007) Cornered drops and rivulets. *Phys. Fluids* 19:042104.

[14] Sokuler M, et al. (2010) The softer the better: Fast condensation on soft surfaces. *Langmuir* 26:1544–1547.

[15] Lavielle N, Asker D, Hatton, BD (2021) Lubrication dynamics of swollen silicones to limit long term fouling and microbial biofilms. *Soft Matter* 17:936–946.

[16] Cai Z, Pham JT (2022) How Swelling, Cross-Linking, and Aging Affect Drop Pinning on Lubricant-Infused, Low Modulus Elastomers. *ACS Appl. Polym. Mater.* 4:3013–3022.

[17] Carré A, Gastel JC, Shanahan MER (1996) Viscoelastic effects in the spreading of liquids. *Nature* 379:432–434.

[18] Long D, Ajdari A, Leibler L (1996) How do grafted polymer layers alter the dynamics of wetting ? *Langmuir* 12:1675–1680.

[19] Style RW, Boltyanskiy R, Che Y, Wettlaufer JS, Wilen LA, Dufresne ER (2013) Universal deformation of soft substrates near a contact line and the direct measurement of solid surface stresses. *Phys. Rev. Lett.* 110:066103.

[20] Park SJ, et al. (2014) Visualization of asymmetric wetting ridges on soft solids with X-ray microscopy. *Nat. Commun.* 5:5369.

[21] Carré A, Shanahan MER (2001) Viscoelastic braking of a running drop. *Langmuir* 17:2982–2985.

[22] Style RW, et al. (2013) Patterning droplets with durotaxis. *Proc. Nat. Acad. Sci. U.S.A* 110:12541–12544.

[23] Karpitschka S, et al. (2016) Liquid drops attract or repel by the inverted Cheerios effect. *Proc. Natl. Acad. Sci. U.S.A.* 113:7403–7407.

[24] Zhao M, et al. (2018) Geometrical control of dissipation during the spreading of liquids on soft solids. *Proc. Nat. Acad. Sci. U.S.A.* 115:1748–1753.

[25] Smith-Mannschott K, et al. (2021) Droplets Sit and Slide Anisotropically on Soft, Stretched Substrates. *Phys. Rev. Lett.* 126:158004.

[26] Khattak HK, Karpitschka S, Snoeijer JH, Dalnoki-Veress K (2022) Direct force measurement of microscopic droplets pulled along soft surfaces. *Nature communications* 13:4436.

[27] Karpitschka S, et al. (2015) Droplets move over viscoelastic substrates by surfing a ridge. *Nat. Commun.* 6:7891.

[28] Dervaux J, Roché M, Limat L (2020) Nonlinear theory of wetting on deformable substrates. *Soft Matter* 16:5157–5176.

[29] Curro JG, Pincus P (1983) A theoretical basis for viscoelastic relaxation of elastomers in the long-time limit. *Macromolecules* 16:559–562.

[30] Style RW, Jagota A, Hui CY, Dufresne ER (2017) Elastocapillarity: Surface tension and the mechanics of soft solids. *Annu. Rev. Condens. Matter Phys.* 8:99–118.

[31] Andreotti B, Snoeijer JH (2020) Statics and Dynamics of Soft Wetting. *Annu. Rev. Fluid Mech.* 52:285–308.

[32] Dussan V. EB, Chow RTP (1983) On the ability of drops or bubbles to stick to non-horizontal surfaces of solids. *J. Fluid Mech.* 137:1–29.

[33] Podgorski T (2000) Ph.D. thesis (Université Paris 6).

[34] Ahmed G, Sellier M, Jermy M, Taylor M (2014) Modeling the effects of contact angle hysteresis on the sliding of droplets down inclined surfaces. *Euro. J. Mech. B* 48:218–230.

[35] Eral HB, 't Mannetje DJCM, Oh JM (2013) Contact angle hysteresis: A review of fundamentals and applications. *Colloid Polym Sci* 291:247–260.

[36] Extrand C, Kumagai Y (1997) An Experimental Study of Contact Angle Hysteresis. *J. Colloid Interface Sci.* 191:378–83.

[37] Dussan V. EB (1985) On the ability of drops or bubbles to stick to non-horizontal surfaces of solids. Part 2. Small drops or bubbles having contact angles of arbitrary size. *J. Fluid Mech.* 151:1–20.

[38] Voinov OV (1976) Hydrodynamics of wetting. *Fluid Dyn.* 11:714–721.

[39] Cox RG (1986) The dynamics of the spreading of liquids on a solid-surface. Part 1. Viscous-flow. *J. Fluid Mech.* 168:169–194.

[40] Shuttleworth R (1950) The surface tension of solids. *Proc. Roy. Soc. A* 63:444–457.

[41] Bonn D, Eggers J, Indekeu J, Meunier J, Rolley E (2009) Wetting and spreading. *Rev. Mod. Phys.* 81:739–805.

[42] Hauer L, Cai Z, Skabeev A, Vollmer D, Pham JT (2023) Phase Separation in Wetting Ridges of Sliding Drops on Soft and Swollen Surfaces. *Phys. Rev. Lett.* 130:058205.

[43] Villegas M, Zhang Y, Abu Jarad N, Soleymani L, Didar TF (2019) Liquid-Infused Surfaces: A Review of Theory, Design, and Applications. *ACS Nano* 13:8517–8536.

[44] Bain N, et al. (2021) Surface tension and the strain-dependent topography of soft solids. *Phys. Rev. Lett.* 127:208001.

[45] Hourlier-Fargette A, Antkowiak A, Chateauminois A, Neukirch S (2017) Role of uncrosslinked chains in droplets dynamics on silicone elastomers. *Soft Matter* 13:3484–3491.

[46] Hourlier-Fargette A, Dervaux J, Antkowiak A, Neukirch S (2018) Extraction of Silicone Uncrosslinked Chains at Air–Water–Polydimethylsiloxane Triple Lines. *Langmuir* 34:12244–12250.

[47] Rubinstein M, Colby RH (2003) *Polymer Physics*. (Oxford University Press Inc., New York, USA).

[48] Curro JG, Pearson DS, Helfand E (1985) Viscoelasticity of Randomly Cross-Linked Polymer Networks. Relaxation of Dangling Chains. *Macromolecules* 18:1157–1162.

[49] Schindelin J, etal. (2012) Fiji: An open-source platform for biological-image analysis. *Nat. Methods* 9:676–682.